Supporting Information

Compact, Robust, Regulated-output Hybrid Generator for Magnetic Energy Harvesting and Self-powered Sensing Applications in Power Transmission Lines

*Qingtong Li [+], Lei Zhang [+, *], Chi Zhang, Yu Tian, Yanyun Fan, Bo Li, Zhengang An, Dachao Li[*], Zhong Lin Wang[*]*

[+] Q. Li and L. Zhang contributed equally to this work.

Q. Li, Prof. L. Zhang, Y. Tian, C. Zhang, Y Fan, B Li, Z An, Prof. D. Li

State Key Laboratory of Precision Measurement Technology and Instruments, Tianjin University, Tianjin, 300072, China.

Prof. Z.L. Wang

Beijing Institute of Nanoenergy and Nanosystems, Chinese Academy of Sciences, Beijing 100083, China.

School of Materials Science and Engineering, Georgia Institute of Technology, Atlanta, GA 30332, United States.

Yonsei Frontier Lab, Yonsei University, Seoul 03722, Republic of Korea.

E-mail: zhangleitd@tju.edu.cn; dchli@tju.edu.cn; zlwang@binn.cas.cn

Content of the Supplementary information

Fig. S1. The detailed preparation process of HMEH.

Fig. S2. The weighing photo of the HMEH, indicating that the weight of the HMEH is 56 g.

Fig. S3. Simulation results of transmission line AC magnetic field. A) AC Magnetic Field Variation at a distance of 0.5 mm from the transmission line. B) Magnetic field strength variation with different cable currents from 200 A to 1000 A.

Fig. S4. Comparison of simulated rotor torque distribution of MMEC module with and without short-circuit rings.

Fig. S5. Dependence of the rotor torque and speed of the MMEC module with different magnet number.

Fig. S6. Simulated rotor torque distribution of MMEC module wtih A) various short-circuit ring diameters, B) various short-circuit ring turns, and C) various short-circuit ring areas.

Fig. S7. Enlarged output signals of EMG module with different magnet number. A) The short-circuit current. B) The open-circuit voltage.

Fig. S8. The output short-circuit current and open-circuit voltage of EMG module with different coil turns.

Fig. S9. The output short-circuit current and open-circuit voltage of EMG module with different coil wire diameters of 0.05 mm and 0.1 mm.

Fig. S10. The output short-circuit current and open-circuit voltage of EMG module with 4 magnets and cable currents range from 100 A to 800 A.

Fig. S11. The output short-circuit current and open-circuit voltage of EMG module with 6 magnets and cable currents range from 100 A to 800 A.

Fig. S12. The output voltage of EMG module with various external loading resistance ranging from 50 Ω-1 GΩ.

Fig. S13. Long-term stability of the EMG module operation for 42 days.

Fig. S14. Charge transfer process of the TENG module in the stable saturation state.

Fig. S15. Enlarged output signals of TENG module with 4 magnets. A) The short-circuit current. B) The open-circuit voltage. C) The short-circuit charge.

Fig. S16. The output voltage of TENG module under various external loading resistance ranging from 50 Ω-1 GΩ.

Fig. S17. Long-term stability of the TENG module operation for 42 days.

Fig. S18. The Q-V Curves of A) EMG, B) EMG with management circuit, C) TENG, D) TENG with management circuit, E) HMEH device within single rotation cycle (50 Hz, 20 ms).

Fig. S19. The V-Q curves of HMEH within per rotation cycle under 1 mm vibration amplitude and different vibration frequencies from 10 Hz to 10 kHz.

Supplement Note S1. Explain the relationship between the number of magnets and the speed of rotation.

Video S1 Demonstration of waterproof test.

Video S2 Demonstration of magnetic phase difference driven magneto-machine conversion process.

Video S3 Demonstration of lighting 500lm LED bulbs.

Video S4 Demonstration of powering calculator.
Video S5 Demonstration of self-powered wireless temperature sensing system

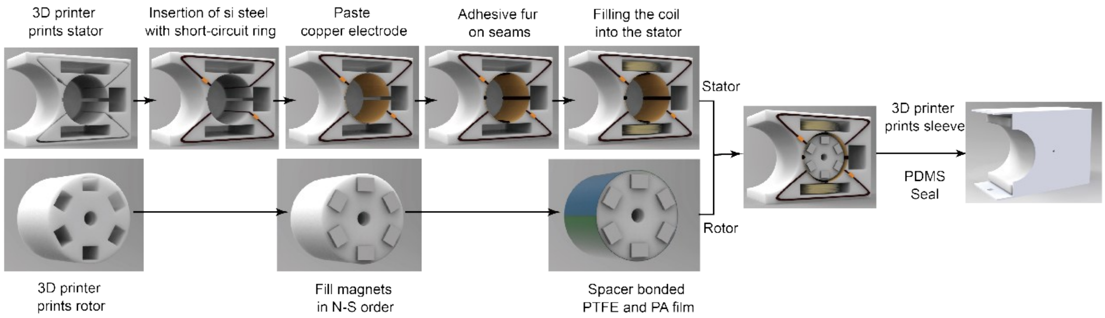

Fig. S1. The detailed preparation process of HMEH.

Fig. S2. The weighing photo of the HMEH, indicating that the weight of the HMEH is 56 g.

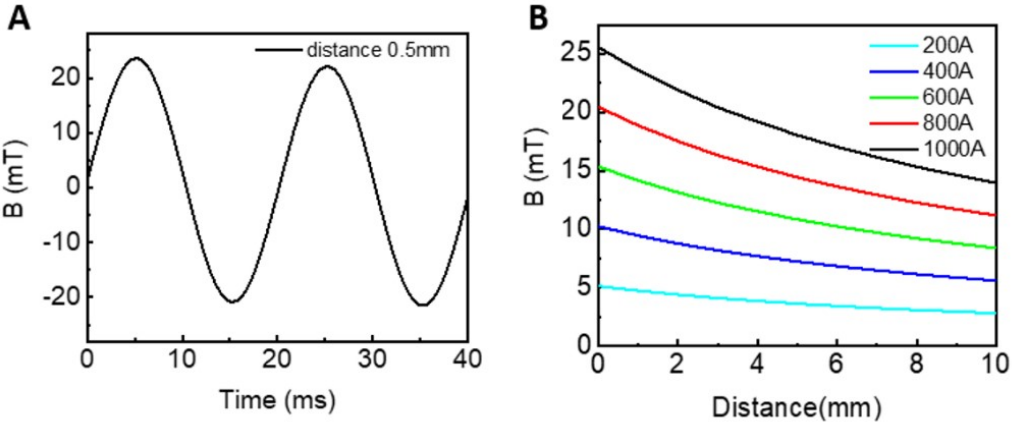

Fig. S3. Simulation results of transmission line AC magnetic field. A) AC Magnetic Field Variation at a distance of 0.5 mm from the transmission line. B) Magnetic field strength variation with different cable currents from 200 A to 1000 A.

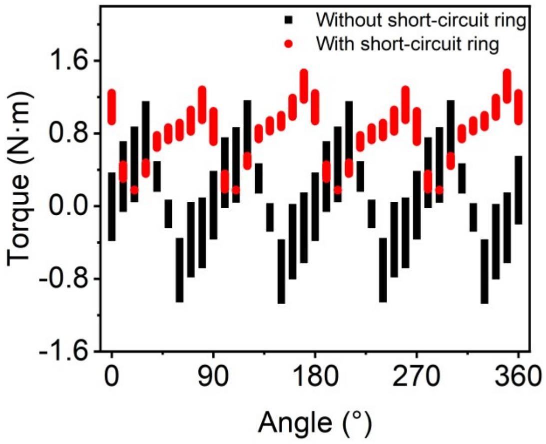

Fig. S4. Comparison of simulated rotor torque distribution of MMEC module with and without short-circuit rings.

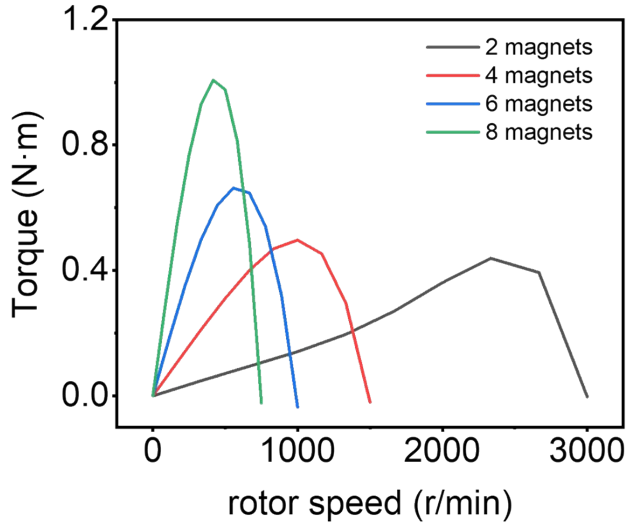

Fig. S5. Dependence of the rotor torque and speed of the MMEC module with different magnet number.

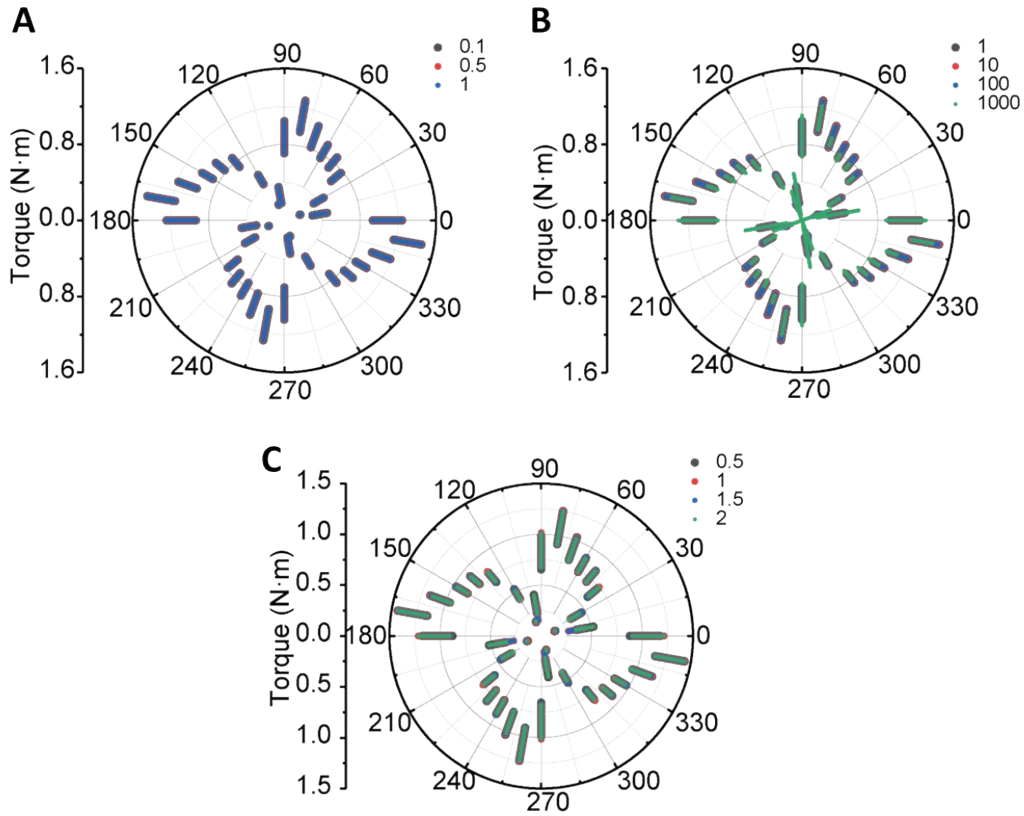

Fig. S6. Simulated rotor torque distribution of MMEC module wtih A) various short-circuit ring diameters, B) various short-circuit ring turns, and C) various short-circuit ring areas.

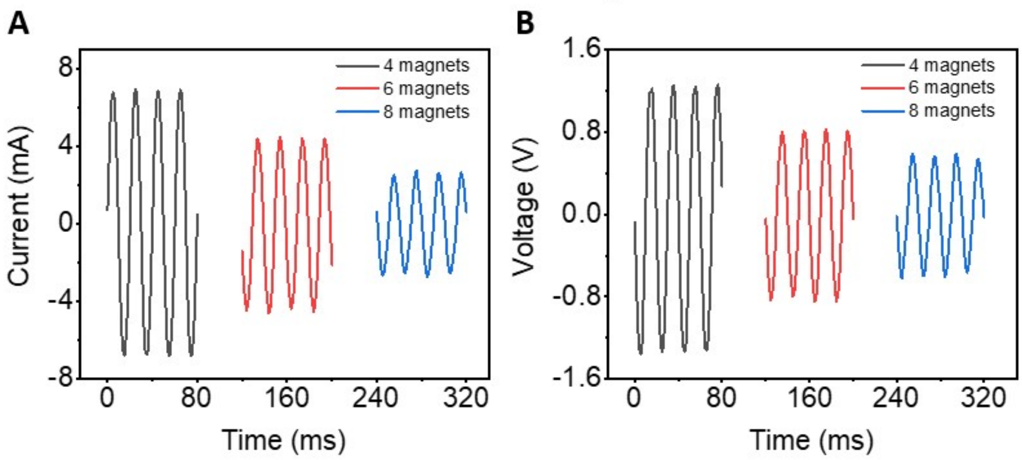

Fig. S7. Enlarged output signals of EMG module with different magnet number. A) The short-circuit current. B) The open-circuit voltage.

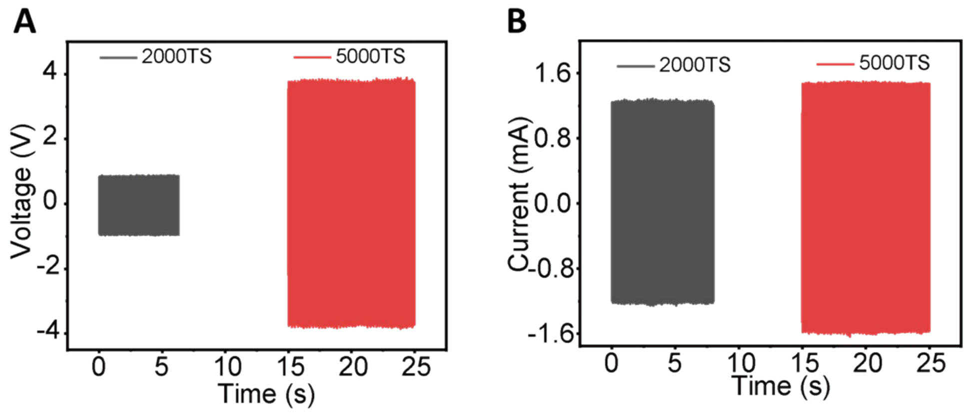

Fig. S8. The output short-circuit current and open-circuit voltage of EMG module with different coil turns.

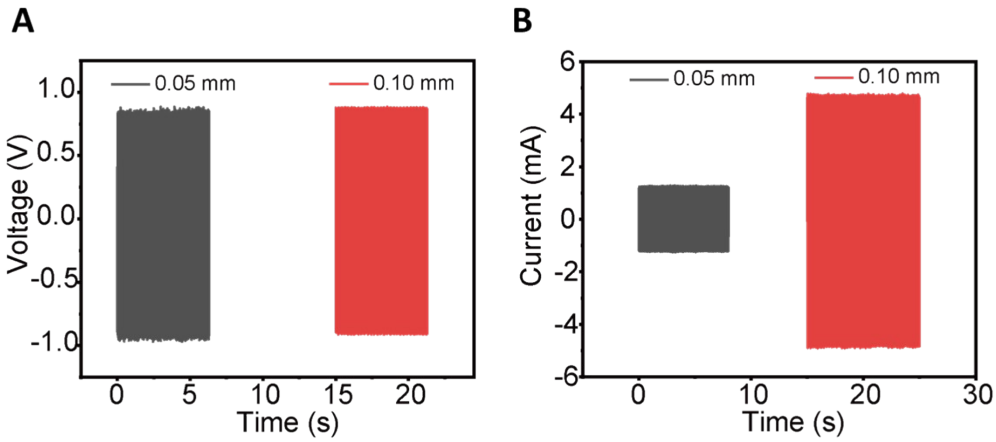

Fig. S9. The output short-circuit current and open-circuit voltage of EMG module with different coil wire diameters of 0.05 mm and 0.1 mm.

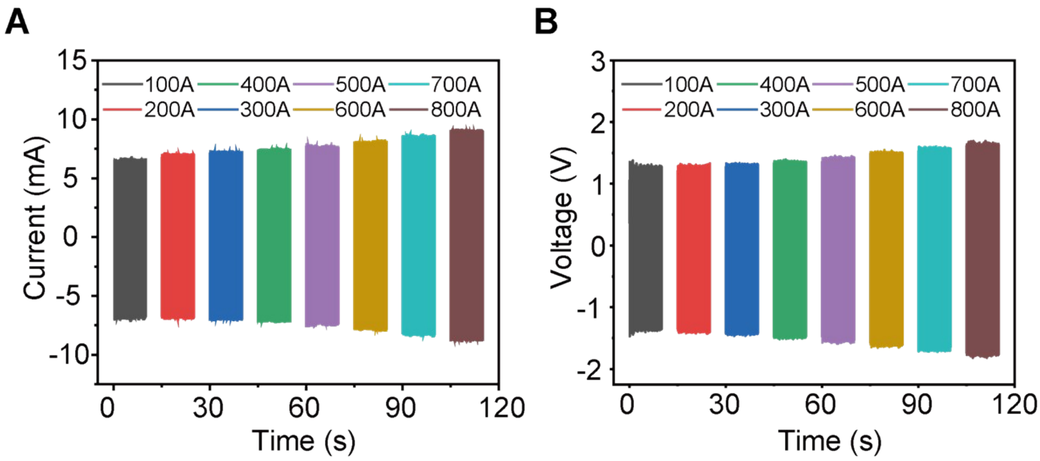

Fig. S10. The output short-circuit current and open-circuit voltage of EMG module with 4 magnets and cable currents range from 100 A to 800 A.

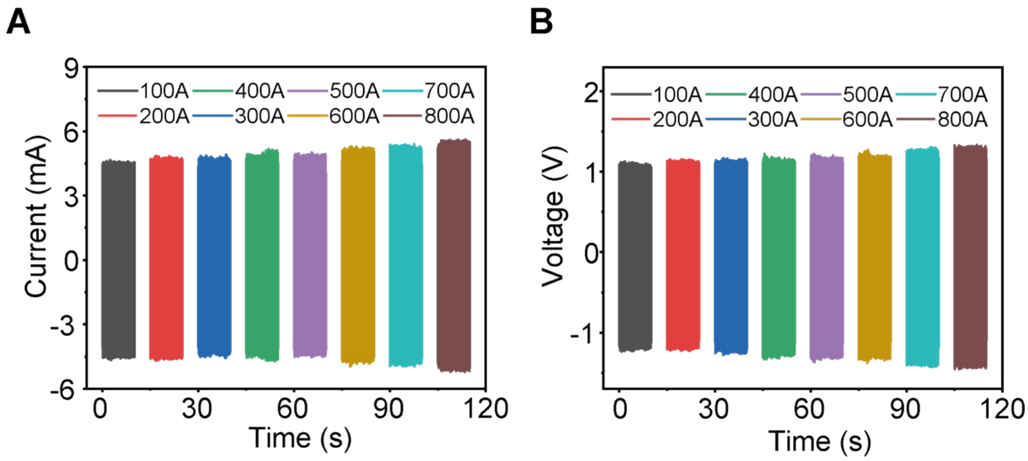

Fig. S11. The output short-circuit current and open-circuit voltage of EMG module with 6 magnets and cable currents range from 100 A to 800 A.

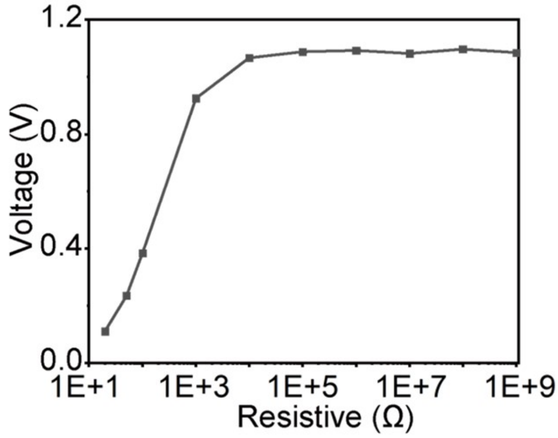

Fig. S12. The output voltage of EMG module with various external loading resistance ranging from 50 Ω-1 GΩ.

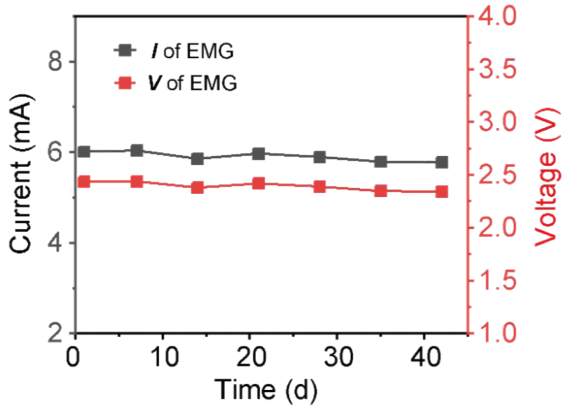

Fig. S13. Long-term stability of the EMG module operation for 42 days.

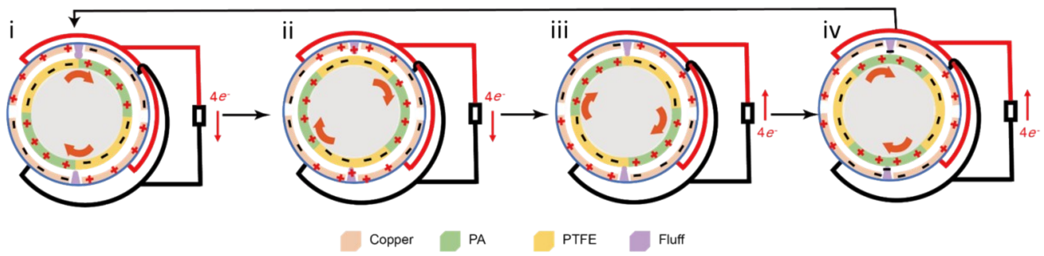

Fig. S14. Charge transfer process of the TENG module in the stable saturation state. i) The rotor comes in contact with the PTFE film covered in polyester fur and shifts by 45°. This results in the PTFE film remaining negatively charged, leading to the induction of zero voltage by the sense electrode, which transfers 4 charges forward. ii) the rotor rotates another 45°, inducing a negative charge from the sense electrode and transferring 4 charges in the forward direction. iii) The object undergoes a 45° rotation, causing the polyester fur to touch the PA film. This maintains the PA's positive charge, inducing a 0 voltage in the sense electrode and transferring 4 charges in the opposite direction. iv) The object then rotates another 45°, leading to a negative charge induction in the sense electrode and 4 charges transferred in reverse.

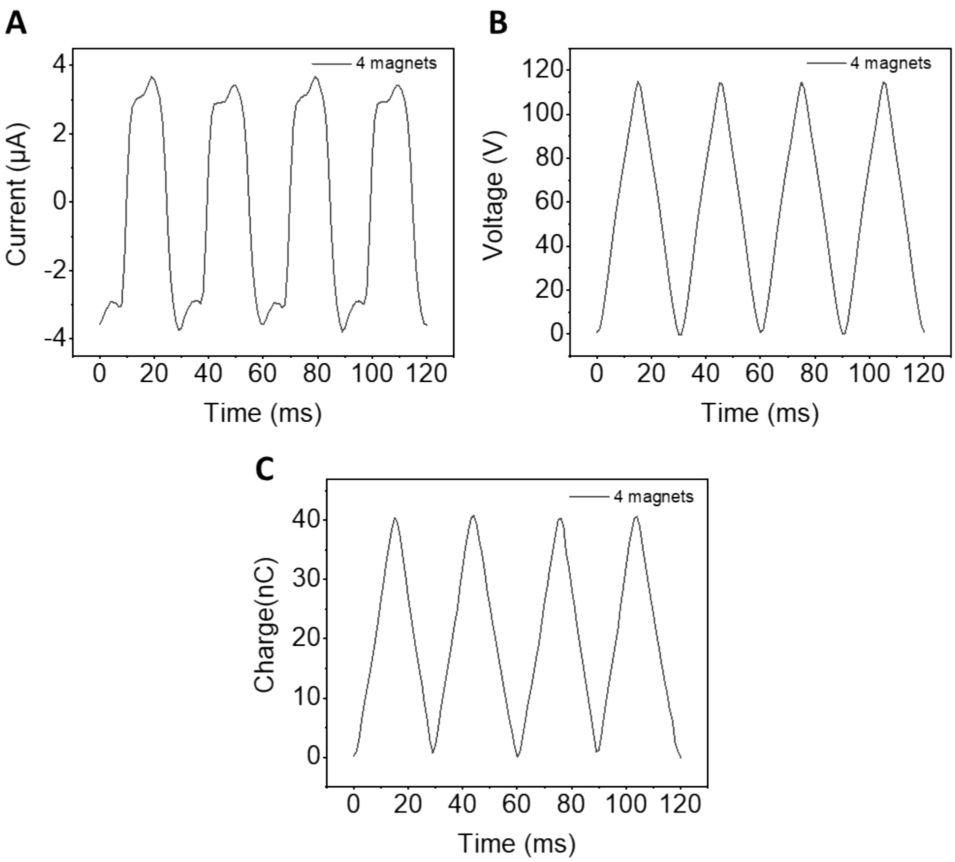

Fig. S15. Enlarged output signals of TENG module with 4 magnets. A) The short-circuit current. B) The open-circuit voltage. C) The short-circuit charge.

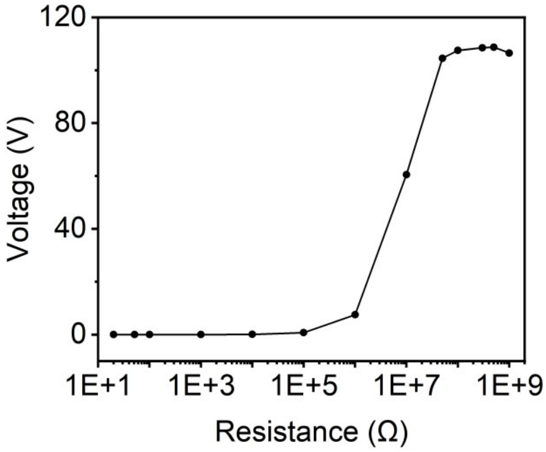

Fig. S16. The output voltage of TENG module under various external loading resistance ranging from 50 Ω-1 GΩ.

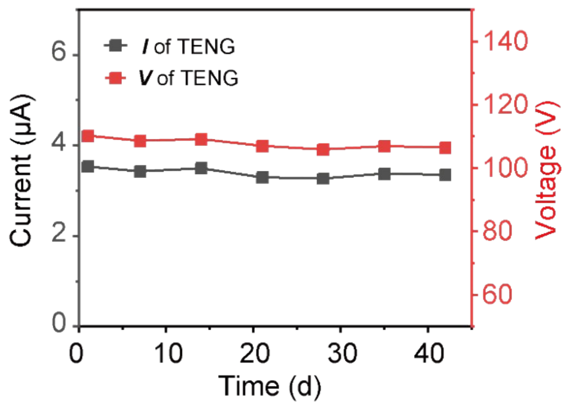

Fig. S17. Long-term stability of the TENG module operation for 42 days.

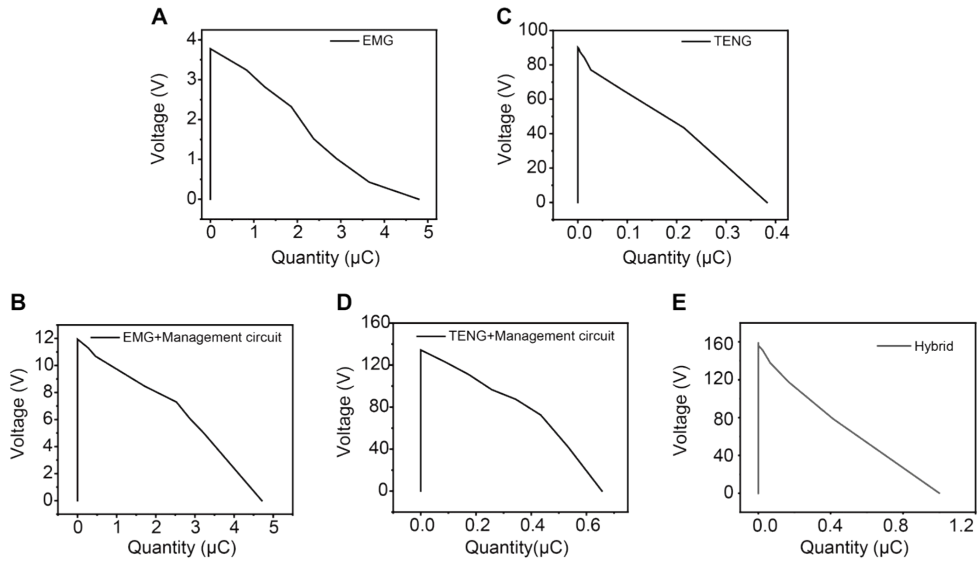

Fig. S18. The Q-V Curves of A) EMG, B) EMG with management circuit, C) TENG, D) TENG with management circuit, E) HMEH device within single rotation cycle (50 Hz, 20 ms).

The output energy, power, and power density of above five additions can be calculated as follow:

- The ***output energy*** within single rotation cycle can be calculated from Equation $E = \int_{0}^{Q_{max}} VdQ$, the detail as follows: A) E_{EMG} =9.12 μJ; B) E_{EMG+MC} =28.8 μJ; C) E_{TENG} = 17.55 μJ; D) $E_{TENG+MC}$ = 45.54 μJ; E) E_{HMEH} = 73.47 μJ.
- The ***output power*** can be calculated from Equation $P=E/t$ ($t=20\ ms$), the detail as follows: A) P_{EMG} =0.456 mW; B) P_{EMG+MC}=1.44 mW; C) P_{TENG} =0.878 mW; D) $P_{TENG+MC}$ =2.277 mW; E) P_{HMEH} =3.67 mW.
- The ***output power density*** can be obtained as follows: A) P_{EMG} =6.08 μW/cm^3; B) P_{EMG+MC}=19.2 μW/cm^3; C) P_{TENG} =11.71 μW/cm^3; D) $P_{TENG+MC}$ =30.36 μW/cm^3; E) P_{HMEH} =48.94 μW/cm^3. The volume of the devices is 75 cm^3 (3 cm*5 cm*5 cm).

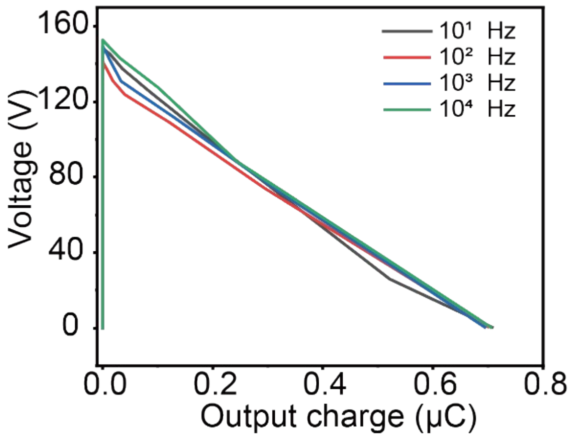

Fig. S19. The V-Q curves of HMEH within per rotation cycle under 1 mm vibration amplitude and different vibration frequencies from 10 Hz to 10 kHz.

Supplement Note S1.

Explain the relationship between the number of magnets and the speed of rotation.

Two crucial concepts are presented initially: the mechanical angle α and the electrical angle β. Mechanical angle α describes the actual rotation angle of the rotor in space, while the electrical angle β is the spatial angle between the magnet pair inside the rotor. The relationship between these two can be expressed using a formula $\beta=\alpha * p$ represents, where p is the number of magnetic pairs.

From an electromagnetic perspective, a rotating magnetic field drives the rotor to rotate, achieving synchronization between the rotating magnetic field and the rotor. This also means that the magnetic field of the rotor will change periodically at the same electrical angle. The consistency of electrical angles reveals an inverse relationship between the maximum speed of the rotor and the number of magnets, that is, an increase in the number of magnets results in a decrease in the maximum speed of the rotor. The relationship between the maximum rotational speed of the sub and the number of magnets can be calculated as:

$S=60 * f/p$

Among them, f represents the power frequency magnetic field frequency (50 Hz), and p represents the number of magnetic poles.

Therefore, for rotors with 4, 6, and 8 magnets, their maximum speeds are approximately 1500 rpm, 1000 rpm, and 750 rpm, respectively.